

www.acsnano.org

# Atomic-to-Mesoscale Twinning Effects and Strain-Driven Magnetic States in an Anisotropic 2D Ferromagnet FePd<sub>2</sub>Te<sub>2</sub>

Shuo Mi, Manyu Wang, Bingxian Shi, Songyang Li, Xiaoxiao Pei, Yanyan Geng, Shumin Meng, Rui Xu, Li Huang, Wei Ji, Fei Pang, Peng Cheng, Jianfeng Guo, and Zhihai Cheng



Cite This: ACS Nano 2025, 19, 34318-34328



**ACCESS** I

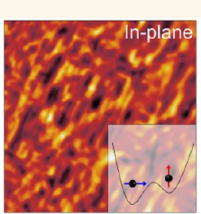
III Metrics & More

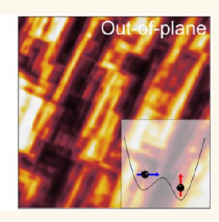
Article Recommendations

s Supporting Information

ABSTRACT: Strain engineering offers a compelling route to modulate magnetism in two-dimensional (2D) materials, yet most approaches rely on externally applied strain. An in-plane anisotropic 2D-layered ferromagnet  $\text{FePd}_2\text{Te}_2$  provides a suitable platform to study intrinsic strain-magnetism coupling due to its twinning domains. Here, we report spatially modulated internal compressive/tensile(C/T) strain regions in  $\text{FePd}_2\text{Te}_2$  and their strong impact on local magnetic properties







in real space by using atomic/magnetic force microscopy (AFM/MFM) combined with scanning tunneling microscopy (STM). Field- and strain-dependent spin transformations reveal the modulation of its intrinsic C/T regions. Notably, C regions retain intact Fe zigzag chains and exhibit larger, abruptly switching magnetic moments, while T regions display fragmented chains with reduced, gradually rotating spins. The intrinsic strain-induced intact ferromagnetic (FM), field-induced polarized-FM states, and their transitions are comparatively discussed during magnetic measurements. Temperature- and field-dependent evolution are further investigated in the FM and paramagnetic (PM) states and summarized to obtain an H-T phase diagram of FePd<sub>2</sub>Te<sub>2</sub>. Our work provides key results for understanding real-space tunable magnetic states through internal structural heterogeneity and suggests potential strategies for manipulating intrinsic strain-engineered magnetic devices.

**KEYWORDS:** vdW materials, twinning domain, structure-dependent magnetism, scanning tunneling microscopy, magnetic force microscopy

Two-dimensional (2D) magnetism has attracted substantial interest in condensed matter physics and spintronics, following the discovery of long-range magnetic order in atomically thin materials such as CrI<sub>3</sub> and Fe<sub>3</sub>GeTe<sub>2</sub>. <sup>1-9</sup> In reduced dimensions, thermal fluctuations tend to suppress the magnetic order. However, magnetic anisotropy, particularly of crystalline origin, can introduce energy barriers that stabilize spin configurations. <sup>2,10-12</sup> Consequently, controlling the anisotropy has become vital for developing functional 2D magnets. Among them, systems with in-plane magnetic anisotropy offer promising opportunities for manipulating spin textures and domain walls, with potential applications for energy-efficient memory and logic devices. <sup>11,13-15</sup>

Strain engineering offers a powerful route to tune magnetic anisotropy, spin orientation, and even Curie temperature without chemical modification. External strain, such as through bending, piezoelectric substrates, or biaxial strain, can dramatically modify magnetic properties in 2D magnets like Fe<sub>3</sub>GaTe<sub>2</sub>, LaCoO<sub>3</sub>, and CrCl<sub>3</sub>. However, few systems naturally host built-in, spatially modulated strain fields capable of tuning magnetism across multiple length scales. Identifying and understanding such intrinsic strain-magnetism coupling

mechanisms is critical not only for low-power control but also for uncovering universal design principles applicable to anisotropic magnetic materials.

 $FePd_2Te_2$  provides a suitable platform to investigate intrinsic strain-driven magnetism.  $^{27-29}$  It combines quasi-1D Fe zigzag chains within a 2D-layered lattice and naturally hosts orthogonal twinning domains where Fe chains rotate by  $90^\circ$  across domain boundaries.  $^{28}$  Unlike conventional extrinsic strain fields, these internal stress domains naturally emerge during growth and persist without external input. Earlier macroscopic work hinted that such twinning domains may influence magnetism,  $^{27}$  but their real-space interplay of intrinsic strain and magnetism remained unresolved.

Received: July 17, 2025 Revised: September 12, 2025

Accepted: September 15, 2025 Published: September 18, 2025





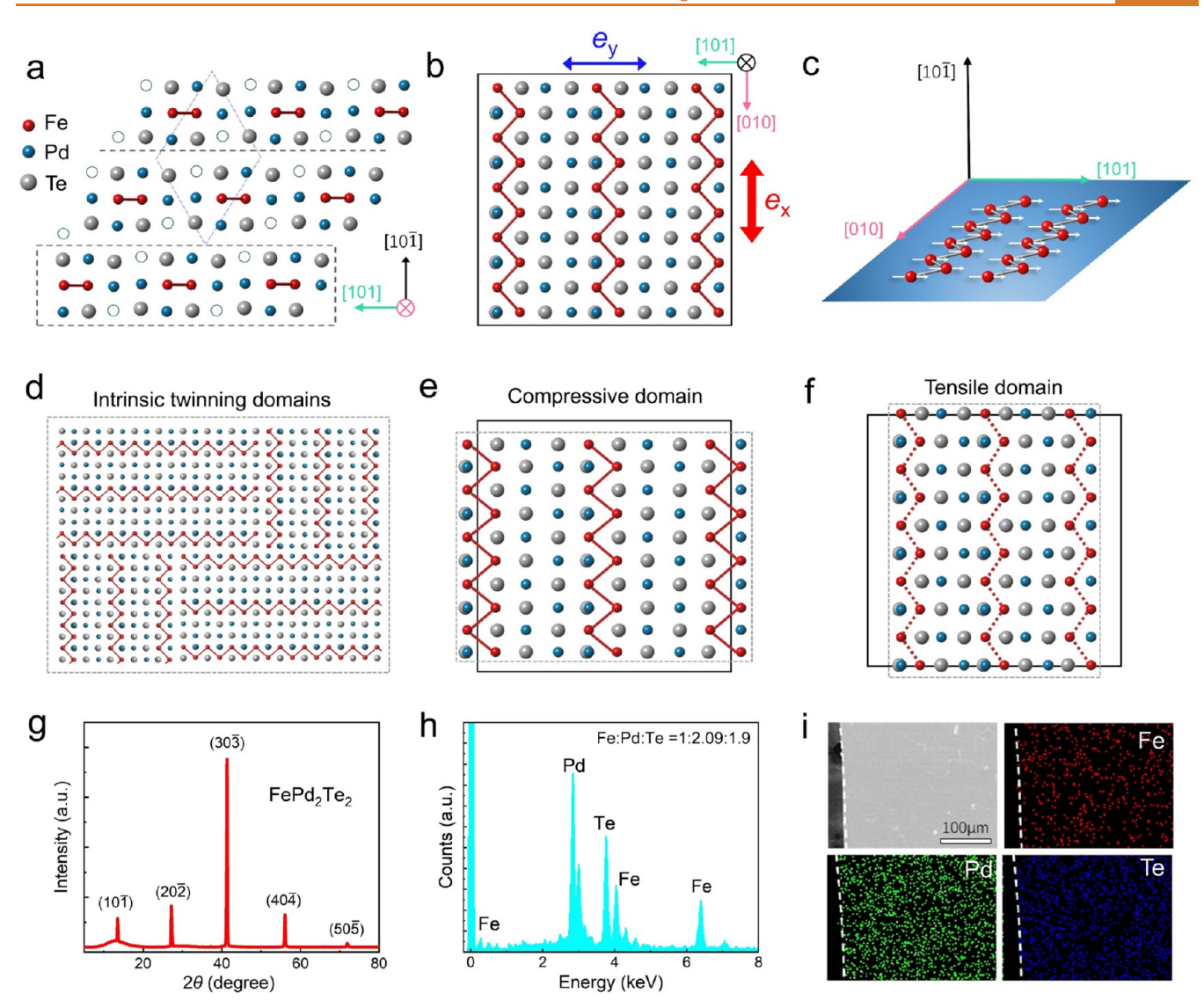


Figure 1. Crystal structures of anisotropic layered  $\text{FePd}_2\text{Te}_2$ . (a,b) Side view (a) and top view (b) of its atomic structure. The crystal structure shows a layered structure along the  $[10\overline{1}]$  directions. The crystal can be easily exfoliated between the Pd-Te layers, as indicated by the black dashed lines. The Fe-zigzag chains lie in the exfoliation (10\overline{10}) plane and along the [010] directions, contributing anisotropic mechanical properties with large  $(e_x)$  along the chain) and small  $(e_y)$  vertical to the chain) Young's modulus. (c) Schematic diagram for the in-plane (vertical to the chain) spin orientations of Fe-chain atoms, indicated by the associated white arrows. (d) Schematic diagram of the coexistent two kinds of domains with orthogonal Fe-zigzag chains. (e,f) Schematics of the compressive (e) and tensile (f) domains after structural relaxation from the unstressed layers of (b) due to their distributed anisotropic domains. The "compressive" and "tensile" refer to lattice distortions along the direction of the Fe-zigzag chains. The red dashed lines in (f) highlight regions where the Fe chains appear disrupted. (g) XRD patterns from the cleavage plane of a FePd<sub>2</sub>Te<sub>2</sub> single crystal. (h,i) EDS elemental analysis (h) and corresponding mapping (i) of one exfoliated FePd<sub>2</sub>Te<sub>2</sub>.

In this work, we show that such intrinsic structural anisotropy in  $FePd_2Te_2$  acts as an internal strain-engineering mechanism, coupling structural domains directly to the local magnetic properties. By combining AFM, STM, MFM, and bulk magnetic measurements, we reveal intrinsic twinning-domain structures in  $FePd_2Te_2$ , characterized by corrugated topography and strain-induced compressive (C) and tensile (T) regions. C regions preserve intact Fe chains and support large, abruptly switching magnetic moments, while T regions exhibit fragmented chains with weaker, gradually reorienting spins. Remarkably, these magnetic domains of C/T regions remain distinguishable even in the field-polarized ferromagnetic (FM) state, indicating a robust intrinsic strain field. Moreover, complex domain evolution is further observed

under varying temperature and field, including a field-polarized paramagnetic (PPM) phase arising from structural corrugation and intrinsic strain. These findings highlight that intrinsic structural heterogeneity can serve as a powerful, internal strain modulator, enabling programmable spin textures and field-tunable magnetic states across temperature scales. This work establishes a perspective for intrinsic strain-engineering in anisotropic van der Waals and quasi-1D materials, offering a foundation for intrinsic strain-engineered spintronic devices and materials.

# **RESULTS**

FePd<sub>2</sub>Te<sub>2</sub> crystallizes in monoclinic  $P2_1/m$  symmetry, with refined unit-cell parameters a = 7.5024(5) Å, b = 3.9534(2) Å,

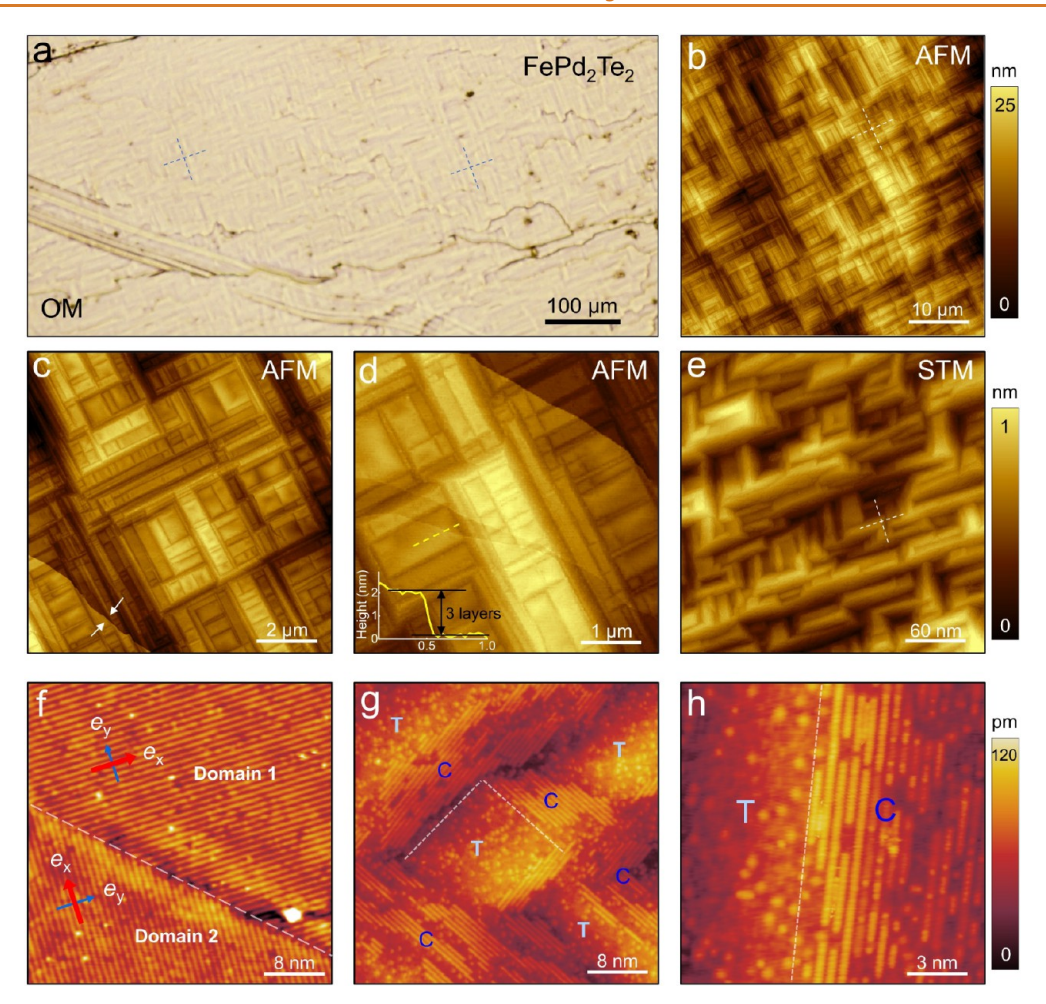


Figure 2. Mesoscale AFM topography and atomic STM structure measurements of  $FePd_2Te_2$ . (a,b) Optical microscopy (a) and large-scale AFM topography images of the freshly cleaved crystal sample with hierarchical orthogonal characteristics. (c,d) Typical AFM topography images of the hierarchical corrugated regions arising from their intrinsic anisotropic twinning domains. (e) Large-scale STM image with hierarchical orthogonal characteristics. (f) STM image of the pristine surface with two stitched twinning domains of orthogonal Fe chains. The domain boundary is highlighted by a dashed white line. The anisotropic mechanical properties are represented by its different Young's modulus (large  $e_x$ , along the chain; small  $e_y$ , perpendicular to the chain). (g) STM image of the C and T domains, indicated by their relatively stable (intact Fe chains) and unstable (broken Fe chains) properties after a short thermal treatment. (h) High-resolution STM image of the intact and broken Fe chains of the surface layer at the C and T domains.

 $c = 7.7366(7) \text{ Å}, \ \alpha = \gamma = 90^{\circ}, \text{ and } \beta = 118.15^{\circ}.^{29} \text{ The cleavage}$ plane (highlighted by dotted lines) occurs along  $(10\overline{1})$ , sandwiched between Pd-Te sublayers (Figure 1a). The triple layer of FePd<sub>2</sub>Te<sub>2</sub> features anisotropic Fe-zigzag chains sandwiched between the top and bottom Pd-Te sublayers, as shown in Figure 1b, which is the origin of anisotropic mechanical properties. The nearest interchain distance is about 7.50 Å, while the intrachain nearest Fe-Fe distance is only 2.68 Å.<sup>29</sup> Due to the crystal structure of FePd<sub>2</sub>Te<sub>2</sub>, atomic bonding is expected to be stronger along the chain direction  $(e_x, parallel to the [010] direction)$ , leading to a relatively large Young's modulus.<sup>30</sup> In contrast, the bonding perpendicular to the chains  $(e_v, \text{ along the } [101] \text{ direction})$ , which involves weaker interchain interactions, results in a much smaller Young's modulus, as illustrated in Figure 1b. These Fe-zigzag chains also dictate the magnetic behavior (Figure 1c), establishing an in-plane easy axis along the [101] direction. Notably, when a sufficiently strong out-of-plane magnetic field is applied, the material can still be polarized along the field direction.<sup>29</sup> However, the in situ real-space evolution of this polarization process has not been explored.

Elastic anisotropy forces FePd2Te2 to exhibit intrinsic orthogonal twinning domains (Figure 1d) due to its quasione-dimensional Fe-zigzag chains embedded in a square Pd-Te lattice. The Fe chains spontaneously orient along two perpendicular in-plane directions, creating 90° rotated twinning domains rather than a uniform single-domain structure to preserve the Te lattice's 4-fold symmetry. This behavior is not mechanically induced but instead reflects a spontaneous release of internal stress arising from the competition between strong intrachain Fe-Fe bonding and weaker interlayer van der Waals interactions. Because of Young's modulus anisotropy, this elastic anisotropy amplifies stress differences, leading to domains of compressive (C) and tensile (T), as shown in Figure 1e,f. Along the Fe-chain direction, tensile strain is more likely to induce chain rupture, and then, the Fe chains in T regions may appear incomplete or disrupted. Such C/T domains arising from intrinsic structural anisotropy may profoundly influence both the lattice architecture and the magnetic behavior of bulk materials.

For instance, in Nd-Fe-B permanent magnets, similar internal stresses alter lattice constants and magnetic texture.<sup>31</sup>

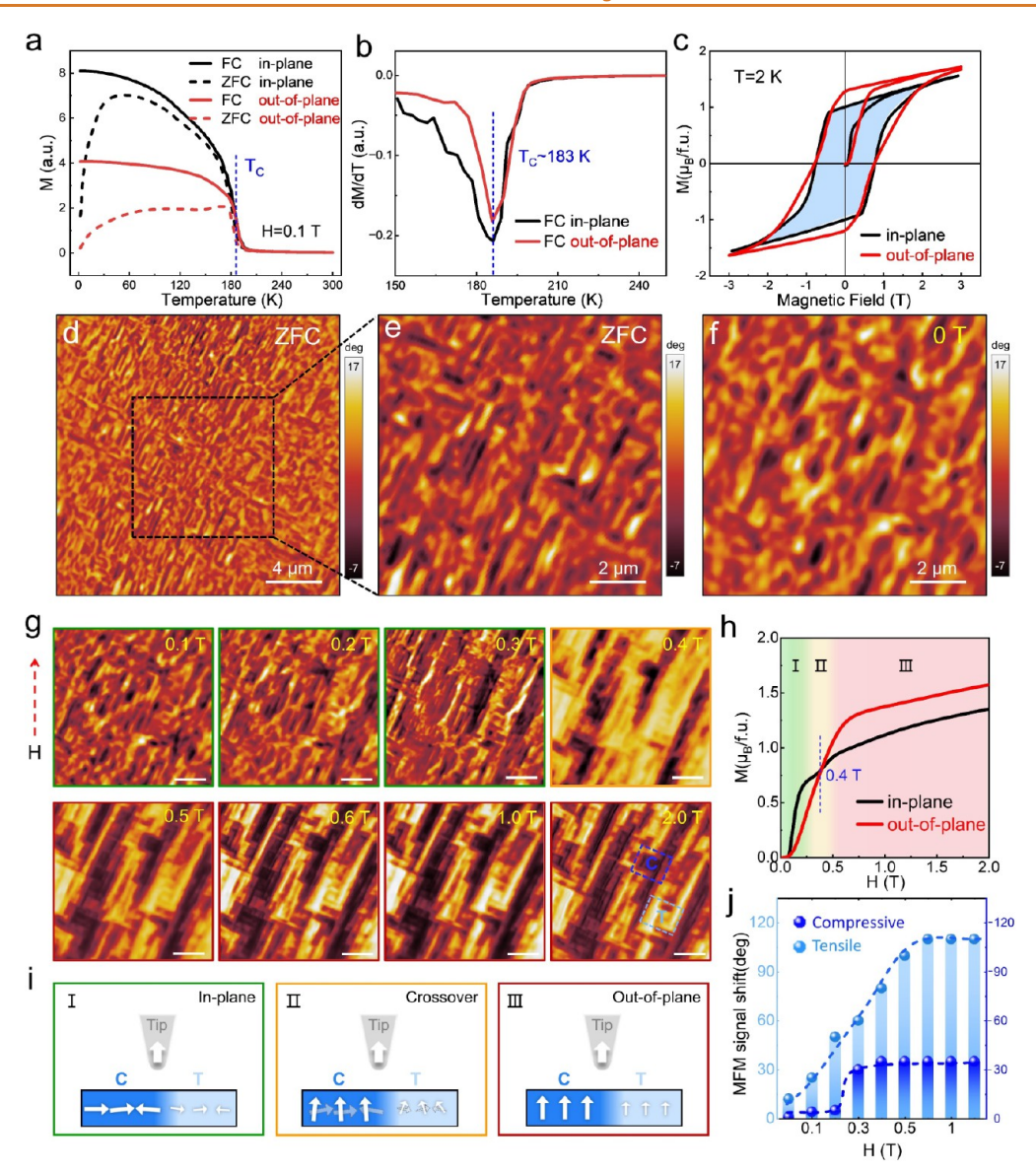


Figure 3. Magnetic properties and MFM measurements of FePd $_2$ Te $_2$ . (a) Temperature-dependent magnetic moments (M-T) with the out-of-plane (red) and in-plane (black) magnetic fields for the FC (solid line) and ZFC (dashed line) processes at 0.1 T. (b) The derivative dM/dT curves from (a). (c) Magnetic hysteresis of out-of-plane (red) and in-plane (black) peaks at 2 K. (d,e) Typical MFM images at ~2 K after zero-field cooling (ZFC) at large (d) and small (e) scales. (f) Typical MFM image at ~2 K after ZFC at 0 T. (g) Field-dependent MFM images of (f) with increased out-of-plane fields at three specific ranges: 0.1–0.3 T (I), ~0.4 T (II), and 0.4–2.0 T (III). (h) Initial M-H curves of out-of-plane (red) and in-plane (black) at 2 K with three highlighted ranges (I, II, and III). A clear crossover from in-plane to out-of-plane field polarization is observed at ~0.4 T. (i) Schematic diagrams of the compressive (C, dark blue) and tensile (T, light blue) domains with large (big arrows) and reduced (small arrows) magnetic moments, respectively, at the three field-polarization ranges (I, II, and III). (j) Field-dependent MFM signal shifts of compressive (C, dark blue) and tensile (T, light blue) regions deduced from (g). The magnetic contrast extraction procedure is detailed in Figure S4.

Many theories also show that local strain can rotate magnetic easy axes, fragment metal chains, or suppress the local moments in low-dimensional Fe systems and related alloys, while high fields can trigger additional spin-flop or spin-flip transitions in layered ferromagnets. Together, these studies suggest that both the intrinsic strain C/T domains and an applied out-of-plane field should cooperatively modulate Fe chain integrity and moment orientation in FePd<sub>2</sub>Te<sub>2</sub>.

Motivated by these considerations, we grew FePd<sub>2</sub>Te<sub>2</sub> crystals to investigate how it modulates. Single crystals of FePd<sub>2</sub>Te<sub>2</sub> were grown by melting stoichiometric elements and were characterized by XRD and EDS measurements. The XRD data in Figure 1g confirm the exfoliated (101) plane of the

synthesized crystal. Further EDS elemental analysis (Figure 1h) and mapping (Figure 1i) confirm the chemical composition of  $FePd_2Te_2$  with a uniform spatial distribution. The successful growth of high-quality crystals lays a solid foundation for subsequent real-space investigations of the material's structural domains and magnetic properties.

The optical microscope image (Figure 1a) displays perpendicularly oriented stripes, tens of micrometers wide, that originate from the intrinsic twinning-domain effect in FePd<sub>2</sub>Te<sub>2</sub>. Figure 2b presents an AFM topography image over the same region, in which the intricate hierarchical structures emerge clearly. These corrugated regions form self-similar, multiscale structures, where small-scale corrugations repeat

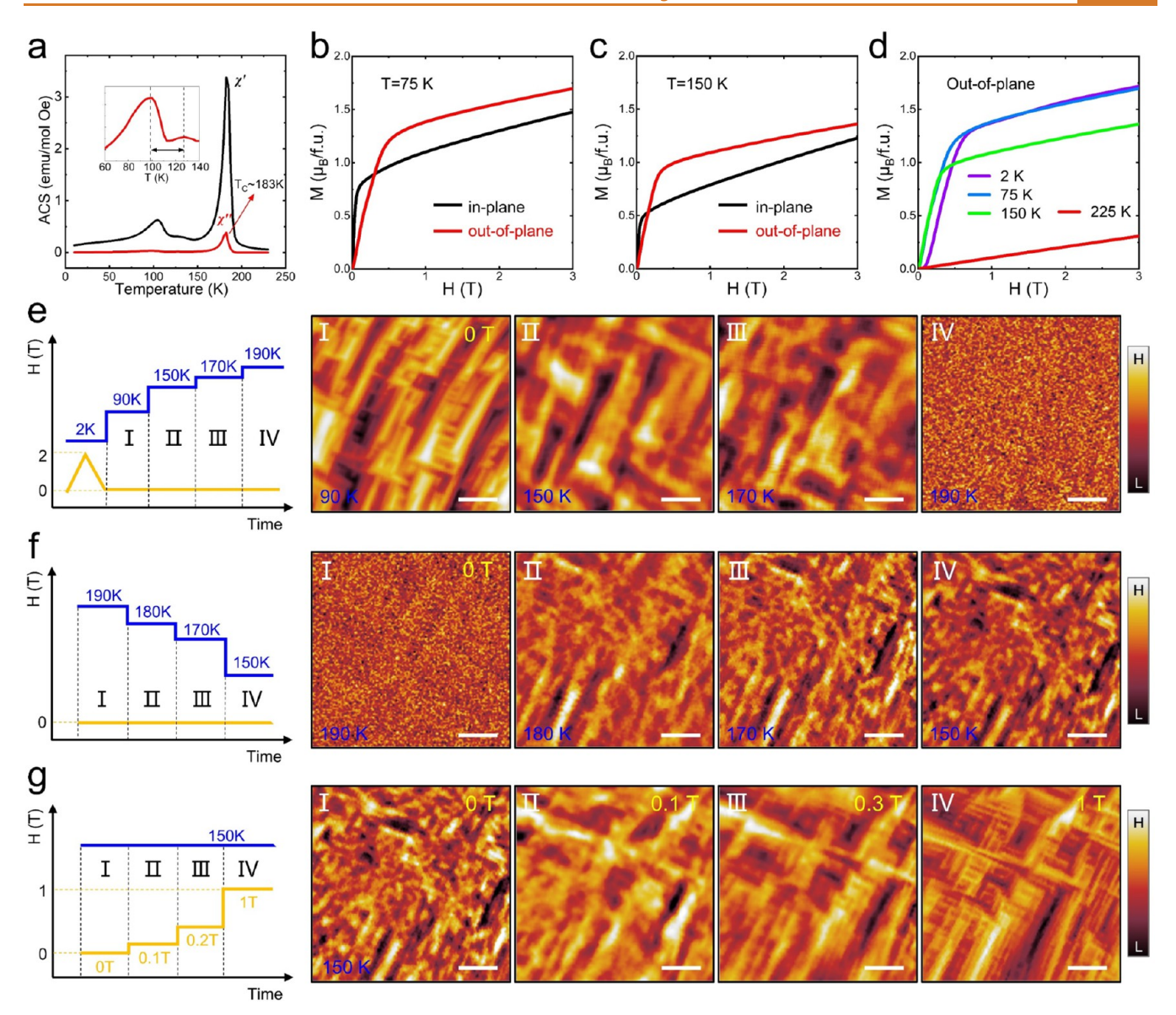


Figure 4. Temperature-dependent magnetic susceptibility and MFM measurements of FePd<sub>2</sub>Te<sub>2</sub>. (a) Temperature-dependent AC magnetic susceptibility measured under a magnetic field, indicating a clear PM-FM transition and a broad magnetic crossover at ~183 K. The inset shows an enlarged view of  $\chi_{ac}^{"}(T)$  at ~100–120 K. (b,c) M-H curves of the out-of-plane (red) and in-plane (black) magnetizations at 75 K (b) and 150 K (c). (d) M-H curves of the out-of-plane magnetization at different temperatures. (e) Temperature-dependent MFM images showing the transition from the polarized-FM to PM state during the zero-field warming process. (f) Temperature-dependent MFM images illustrating the transition from the PM to FM state during the zero-field cooling process. (g) Field-dependent MFM images showing the transition from the FM to polarized-FM state at ~150 K.

within larger stripe domains. Medium-scale AFM images (Figure 2c,d) show a layered surface with clear step edges (white arrows), confirming the layered structural characteristic. Each layer exhibits periodic vertical heights of  $\sim 10$  nm (Figure S2) that continue seamlessly across neighboring layers. Specifically, these features are highly reproducible across multiple cleaved flakes and distinct samples, confirming that the hierarchical structure is an intrinsic characteristic of FePd<sub>2</sub>Te<sub>2</sub> rather than a sample-specific artifact. We attribute these corrugations to structural relaxation driven by anisotropic stress within orthogonal twinning domains. The anisotropic Fe-zigzag chains drive these stress fields and mediate the resulting topographic modulation.

Low-temperature STM ( $\sim$ 10 K) further elucidates the structure. The large-area STM image in Figure 2e is consistent

with medium-scale AFM images, while Figure 2f resolves two domains with orthogonal Fe-chain orientations separated by a sharp twin boundary. Thermal treatment reveals the internal stress distribution, manifesting two types of regions with either intact or disrupted Fe chains. Based on prior reports, tensile strain destabilizes atomic chains, whereas compressive strain tends to preserve their integrity.<sup>32–35</sup> Accordingly, we identify the regions with intact Fe chains as C regions, while the regions exhibiting chain rupture are assigned as T regions (Figure 2g). Domain boundaries between C and T regions appear topographically as convex ridges or concave valleys (see details in Figure S3). Figure 2h highlights a convex ridge demarcating a C region with continuous Fe chains from a T region with broken chains (Figure S4).

These observations collectively demonstrate that  $FePd_2Te_2$  shows complex hierarchical structural features extending from the atomic to the mesoscale. The corrugated surface topography, the emergence of C and T regions, and the formation of distinct boundaries all stem from its intrinsic anisotropy and twinning-domain architecture. These structural inhomogeneities are not merely topographical; they are expected to play a significant role in modulating the spin configurations and governing the material's magnetic behavior. To further explore these effects, high-sensitivity MFM measurements should be performed in real space, complemented by conventional magnetic susceptibility characterizations.

Figure 3a presents temperature-dependent magnetization curves measured under a 0.1 T magnetic field for both in-plane (black) and out-of-plane (red) directions. A clear paramagnetic-ferromagnetic (PM-FM) transition occurs around 180 K, with stronger in-plane magnetization, indicating in-plane ferromagnetic anisotropy. The Curie temperature,  $T_{\rm C}$  = 183 K, determined from the minimum in dM/dT in Figure 3b, shows no orientation dependence. Figure 3c displays the magnetic hysteresis (M-H) loops at 2 K for both directions. The pronounced hysteresis in both directions indicates domain stabilization and confirms hard magnetic behavior.  $^{37,38}$ 

To reveal how the intrinsic twinning effect affects local magnetic behavior in real space, we performed MFM measurements after zero-field cooling (ZFC). The large-area image in Figure 3d shows orthogonal magnetic-contrast patterns. A higher-resolution MFM image (Figure 3e) reveals magnetic domains that are significantly finer than the underlying topographic features, indicating a spin structure more complex than the structural pattern suggests. Fielddependent MFM images after ZFC (Figures 3f,g and S5) can be distinguished into three specific ranges  $(0-0.3 \text{ T}, \sim 0.4 \text{ T})$ and 0.5-2 T), which correspond directly to features observed in the low-temperature M-H hysteresis (Figure 3h). Notably, the M-H curves cross around 0.4 T, indicating a crossover from in-plane magnetization below this field to out-of-plane magnetization above it. This transition is further confirmed in the MFM images. Comparing the MFM contrast at 0 T and 2 T on the same topographic scale shows that low-field domains are much smaller and more intricate, while high-field domains at 2 T clearly match the topographic scale (Figure S5). Furthermore, a sudden emergence of additional domain contrast at ~0.4 T coincides with the M-H crossover. At 0-0.3 T, the in-plane spin moments within twinning domains begin to flop toward the out-of-plane direction, and structural contrast becomes progressively visible. 39,40 Importantly, at 0.5-2 T, the MFM contrast gradually stabilizes and remains unchanged with a further field increase, which we identify as the saturated state. Additional confirmation comes from reversed-field measurements (Figure S4), where the contrast flips direction between -1.4 T and -2 T but remains invariant above -2 T, symmetrically mirroring the behavior at +2 T. This symmetric, field-invariant contrast demonstrates that the system reaches saturation at ~2 T. After removing the field, the spins remain oriented out-of-plane, demonstrating a stable, field-induced polarized state (Figure S4). These observations demonstrate that spin orientation in FePd<sub>2</sub>Te<sub>2</sub> transitions from in-plane to out-of-plane as the external magnetic field increases, with a detailed discussion of this evolution provided in Figure S6.

Unlike typical ferromagnets, however, the MFM images of FePd<sub>2</sub>Te<sub>2</sub> retain a pronounced domain-dependent contrast even in this saturated state. This persistent contrast arises from intrinsic strain-induced differences between C and T regions, which host Fe chains with distinct spin configurations and unequal magnetic moments. Thus, the high-field state represents a polarized-FM phase rather than a uniform single-domain configuration. Previous studies have shown that tensile strain can fragment Fe chains and reduce their local moments, 24-27 allowing us to assign bright/dark contrasts to T/C domains, respectively, as illustrated by the large and small arrows in Figure 3i. The field-dependent evolution of these regions is summarized in Figure 3j as revealed by magnetic contrast (details of MFM image acquisition in Figure S7). Interestingly, as the applied field increases, spins in T domains rotate gradually, while C domains exhibit abrupt, spin-flip-like transitions and reach magnetic saturation at lower fields, 4,5 providing direct evidence of strain-modulated magnetic responses, reflecting distinct magnetic responses between strain-induced C and T regions. The schematics shown in Figure 3i illustrate the evolution of spin configurations in different strain regions throughout the entire magnetic field evolution process. These field- and strain-dependent spin transformations demonstrate that intrinsic twinning-effectinduced C/T strain regions actively orchestrate localized magnetic behavior, enabling complex yet reproducible spin reorientations across multiple length scales.

To elucidate the temperature-dependent magnetic behavior of FePd<sub>2</sub>Te<sub>2</sub>, we performed systematic AC magnetic susceptibility (ACS) measurements and in situ magnetic force microscopy (MFM) imaging. As shown in Figure 4a, ACS measurements exhibit a sharp peak at ~183 K, marking the PM-FM transition, and a broad feature in the 100-120 K range, indicating domain evolution driven by competing thermal fluctuations and magnetic anisotropy. 41 Complementary initial M-H curves at 75 and 150 K (Figure 4b,c) reveal distinct temperature-dependent magnetic anisotropy. With increasing temperature, the distinction between in-plane and out-of-plane responses progressively diminishes, beginning to approach isotropic magnetic behavior. The temperature evolution of the out-of-plane M-H curves from 2 to 225 K reveals an enhancement of out-of-plane magnetic anisotropy in FePd<sub>2</sub>Te<sub>2</sub> (Figure 4d).

To directly visualize the magnetic domain evolution in FePd<sub>2</sub>Te<sub>2</sub>, MFM measurements were performed under three distinct processes (Figure 4e-g), as detailed in the left flowchart. Starting in a polarized-FM state at 2 K, the magnetic contrast gradually fades, and the contrast difference decreases from  $\sim 140^{\circ}$  in the fully out-of-plane state to  $\sim 15^{\circ}$ , eventually disappearing near 190 K (Figures 4e and S8), matching the Curie temperature ( $\sim$ 183 K). Even as the contrast blurs, some domain contrast persists down to ~120 K, aligning with observations of increased magnetic fluctuations in the broad ACS feature. Subsequently, ZFC through the transition restores orthogonal in-plane domain patterns (Figures 4f and S9) similar to those seen at 2 K, confirming that these domains are intrinsically linked to the in-plane twinning structure. Applying an external field during cooling accelerates spin alignment, enabling the system to reach a homogeneous polarized-FM state (Figure S10). As shown in Figure 4g (see also Figure S11), at an intermediate temperature (before and after the fluctuation regime), applying out-of-plane magnetic fields induces a more rapid transition into the polarized-FM

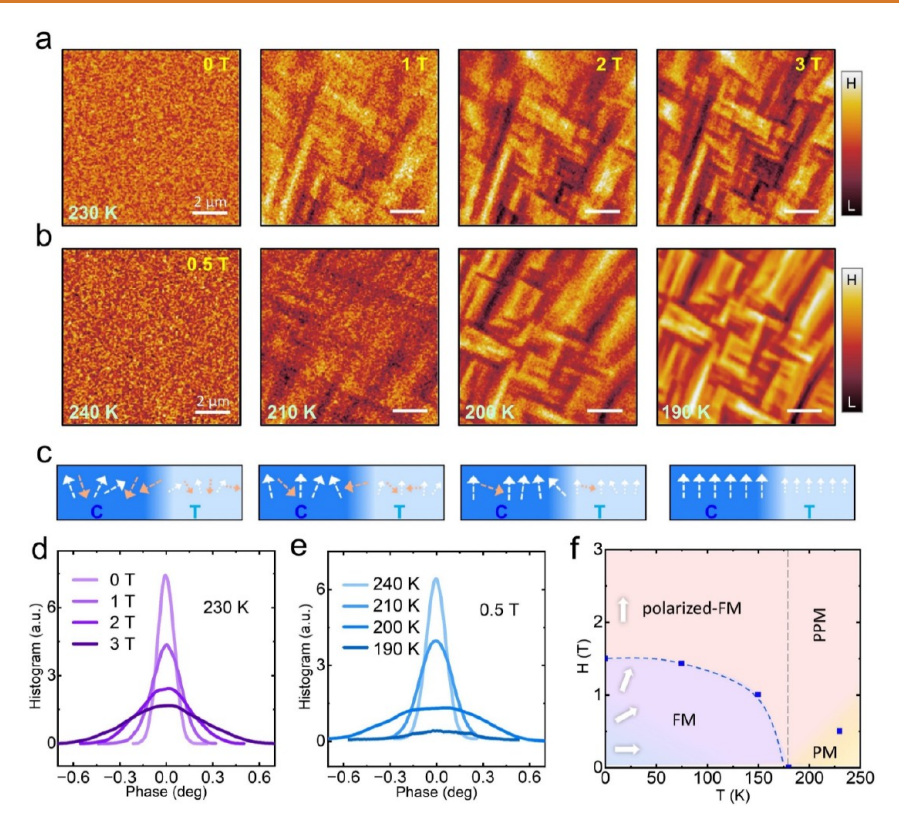


Figure 5. Field-polarized spin textures at the PM state of FePd<sub>2</sub>Te<sub>2</sub>. (a) Field-dependent MFM images showing the transition from the PM to polarized-PM state at 230 K. (b) Temperature-dependent MFM images after field cooling under 0.5 T, illustrating the transition from PM to polarized-FM state. (c) Schematic diagrams of the polarized-PM state with the field-polarized magnetic moments of Fe atoms at the compressive (C, dark blue) and tensile (T, light blue) regions, respectively. (d) Histogram of MFM images in (a). (e) Histogram of MFM images in (b) at different temperatures under a magnetic field of 0.5 T. (d,e) Histograms of MFM images in (a) and (b), respectively. (f) H-T phase diagram of FePd<sub>2</sub>Te<sub>2</sub>, showing the FM (purple), polarized-FM (pink), and PM/field-polarized PM (PPM) state (gradient pink).

state than at low temperature, indicating reduced magnetic anisotropy.

Overall, the ACS and MFM images provide a coherent depiction of magnetic evolution in FePd<sub>2</sub>Te<sub>2</sub>. From ~120 to ~180 K, long-range ferromagnetic order exists with relatively weak anisotropy, enabling easy spin polarization by external fields. Near 100–120 K, thermal energy rivals the anisotropy barrier, enhancing spin fluctuations and causing partially reoriented or dynamic domains. <sup>42–45</sup> Below ~100 K, increased magnetic anisotropy, likely due to coupling with structural domains, requires stronger fields to reorient the spins. These findings highlight the temperature-dependent tuning of magnetic anisotropy and spin textures in FePd<sub>2</sub>Te<sub>2</sub>.

In the conventional PM state, magnetic materials typically lack spontaneous long-range magnetic order. 46,47 Individual spins rapidly randomize, so even when a magnetic field is applied, alignment only occurs transiently, and any local magnetization averages out, yielding no domain contrast. However, in FePd<sub>2</sub>Te<sub>2</sub>, a clear structure-related magnetic contrast emerges in the PM state under an applied field (Figures 5a,b,S12 and S13). At 230 K, the magnetic contrasts are gradually visualized with increased magnetic fields, which is similar to the polarized-FM states (below  $T_c$ ) and can be defined as a field-polarized PM (PPM) state. Notably, this contrast originates from intrinsic differences in the magnetic moments of C and T regions, as previously described, rather than representing a thermodynamic phase. Importantly, when the applied field is removed, the system immediately returns to the conventional PM state without any detectable magnetic

contrast (Figure S10h). A similar evolution occurs under a 0.5 T FC from 240 to 190 K (Figure 5a), where structure-related magnetic domains gradually develop, as shown in the MFM images in Figure 5a. Figure 5c schematically illustrates the magnetic moment's behaviors observed in Figure 5a,b, where similar domain features emerge either by increasing the magnetic field or decreasing the temperature in the PM state.

This behavior can be semiquantitatively described by the Boltzmann distribution, reflecting the competition between thermal fluctuations, which randomize spin orientations, and Zeeman energy, which promotes spin alignment along the magnetic field. Figure 5d,e further supports this interpretation by showing histograms of the MFM phase extracted from the corresponding images in Figure 5a,b, respectively, highlighting the same behavior of the gradual emergence of magnetic contrast under increased fields or decreased temperatures. The comprehensive magnetic phase diagram in Figure 5f summarizes the various magnetic states observed in FePd<sub>2</sub>Te<sub>2</sub>, including the complex FM state, the polarized-FM state, and the PPM state.

## **DISCUSSION**

Our study demonstrated that FePd<sub>2</sub>Te<sub>2</sub> intrinsically forms orthogonal twin domains due to elastic anisotropy, generating internal compressive and tensile regions that control Fe-chain integrity. Using a combination of AFM, STM, MFM, and magnetic susceptibility techniques, we show that T regions exhibit weakened local magnetic moments and gradual spin-flop behavior, while C regions retain intact chains, larger

moments, and abrupt spin transitions. This internal stress-driven modulation leads to a rich, temperature- and field-dependent magnetic phase scale, field-polarized FM, thermally fluctuating domain states, and even a PPM phase above  $T_{\rm C}$ . These findings imply that internal strain fields alone, without any external mechanical manipulation, are sufficient to create and control complex spin textures. Compared with externally applied strain, which typically requires complex device fabrication and an artificial control process, the built-in elastic anisotropy in FePd<sub>2</sub>Te<sub>2</sub> provides a natural and spatially tunable mechanism. This intrinsic stress, therefore, offers a robust platform for exploring strain-magnetism coupling at the atomic scale. Quantitatively linking internal stress to magnetic behavior remains a compelling direction for future work.

From a materials design perspective, the ability to artificially predefine the positions of C and T regions would be highly desirable for device applications such as programmable spin textures or domain-wall-based logic. However, the intrinsic twinning effect of FePd<sub>2</sub>Te<sub>2</sub> currently prevents large-area single-domain crystal growth, limiting our control to local domains. We are, therefore, experimenting with strategies such as tuning elemental ratios, controlled doping, and postgrowth annealing to modulate the formation and distribution of C/T regions. While full deterministic control has not yet been achieved, these approaches may enable partial suppression of twinning and tailored domain architectures in the future.

#### **CONCLUSIONS**

In summary, combined AFM/STM/MFM data provide direct, atomic-scale evidence that internal structural inhomogeneity modulates magnetic properties on the nanoscale. Our work demonstrates the important role of intrinsic elastic strain in tuning magnetic behavior at the atomic scale, without external strain. This provides avenues to design 2D magnetic materials and devices where control over strain domains could enable programmable spin textures and switchable magnetic states. Future efforts should focus on high-resolution MFM/STS mapping across individual C and T domains and strain engineering via targeted lattice deformation. These strategies could lead to functional applications in strain-controlled spintronics and domain-patterned magnetic architectures.

# **METHODS**

Sample Preparation and Characterization. Single crystals of FePd<sub>2</sub>Te<sub>2</sub> were grown by melting stoichiometric elements. Iron, palladium, and tellurium powders were mixed and ground in a molar ratio of 1:2:2. Deviation from this ratio would lead to the unsuccessful growth of large single crystals or the target phase. Then, the mixtures were placed in an alumina crucible and sealed in a quartz tube under vacuum conditions. The entire tube was heated in a box furnace to 800 °C and held at that temperature for 2 days. Then, it was cooled to 600 °C at a rate of 2 °C/h followed by annealing at this temperature for 2 days before being furnace-cooled to room temperature. In addition, we found that quenching the samples at 600 °C would improve the crystal quality, as revealed by X-ray characterization. However, direct quenching during the initial growth process seems to break the large crystal into small pieces. By reannealing and quenching the large single crystals grown by the initial furnace-cooled method, one could obtain crystals with both large size and good quality.

**Structure and Composition Characterization.** The structure of FePd<sub>2</sub>Te<sub>2</sub> crystals was analyzed at 273 K by XRD (D8 ADVANCE, Bruker) equipped with a multilayer mirror monochromated Mo K $\alpha$  ( $\lambda=0.71073$  Å) radiation source. The elemental composition and distribution were evaluated by EDS (X-MaxN 50 mm², Oxford Instruments) in the SEM.

**Magnetic Property Measurements.** The measurements of magnetic susceptibility and  $T_{\rm C}$  were performed using a magnetic property measurement system (MPMS3, Quantum Design), in which the anisotropic magnetic properties of the samples were observed separately. The temperature-dependent magnetic susceptibility for out-of-plane and in-plane magnetic fields was measured within the temperature range of 1.8 to 300 K by the processes of ZFC and FC with a field of 0.1 T, respectively. The field-dependent magnetization studies were performed with an applied field range of 0 to 7 T at temperatures of 2, 75, 150, and 225 K for both out-of-plane and in-plane orientations. Besides, the measurement was performed in DC mode, in which the samples were scanned vertically over 30 mm in 4 s, and the gradients of magnetic field and temperature were set to 100 Oe s<sup>-1</sup> and 2 K min<sup>-1</sup> with the same intervals of 100 Oe and 0.2 K, respectively.

AFM and MFM Measurements. The AFM experiments were performed using a commercial atomic force microscope (Park, NX10) equipped with a commercial topography tip (Nanosensors, AC160TS, quality factor ~500 at room temperature). The scanning probe system was operated at the resonance frequency, ~301 kHz, of the topography tip. The AFM images were acquired in noncontact mode. The MFM experiments were conducted using a commercial magnetic force microscope (attoAFM I, attocube) employing a commercial magnetic tip (Nanosensors, PPP-MFMR, quality factor ~1800 at 2 K) based on a closed-cycle He cryostat (attoDRY2100, attocube). The scanning probe system was operated at the resonance frequency, ~75 kHz, of the magnetic tip. The MFM images were captured in constant-height mode with the scanning plane nominally ~100 nm above the sample surface. The MFM signal, i.e., the change in the cantilever phase, was proportional to the out-of-plane stray field gradient. The dark (bright) regions in the MFM images represented strong (weak) attractive magnetization, corresponding to regions with larger (smaller) magnetic moments. The MFM signal primarily reflects magnetic structures near the sample surface rather than the topmost atomic layer, as it originates from the stray field extending above the surface. Owing to the gradual spatial decay of magnetic dipolar interactions ( $\sim 1/r^2$ ), the tip can sense contributions from a subsurface volume. With a lift height of ~100 nm, the signal mainly represents magnetic domains within approximately the top 100 nm of the sample.4

**STM Characterization.** The samples were cleaved at room temperature and LN<sub>2</sub> temperature in ultrahigh vacuum at a base pressure of  $2\times 10^{-10}$  Torr and directly transferred to the STM system (PanScan Freedom, RHK). Chemically etched Pt–Ir tips were used for STM measurements in constant-current mode at  $\sim 10$  K. The tips were calibrated on a clean Ag(111) surface. Gwyddion was used for the STM data analysis.

#### **ASSOCIATED CONTENT**

## **Data Availability Statement**

The authors declare that the data supporting the findings of this study are available within the article and its Supporting Information.

## Supporting Information

The Supporting Information is available free of charge at https://pubs.acs.org/doi/10.1021/acsnano.5c12067.

Details of AFM, STM, and MFM images, including H-dependent magnetic states, the transition of spin orientation, and the states from polarized-FM to PM, etc (PDF)

### **AUTHOR INFORMATION**

#### **Corresponding Authors**

Zhihai Cheng — Key Laboratory of Quantum State Construction and Manipulation (Ministry of Education), School of Physics, Renmin University of China, Beijing 100872, China; Beijing Key Laboratory of Optoelectronic Functional Materials & Micro-nano Devices, School of Physics, Renmin University of China, Beijing 100872, China; orcid.org/0000-0003-4938-4490; Email: zhihaicheng@ruc.edu.cn

Peng Cheng — Key Laboratory of Quantum State
Construction and Manipulation (Ministry of Education),
School of Physics, Renmin University of China, Beijing
100872, China; Beijing Key Laboratory of Optoelectronic
Functional Materials & Micro-nano Devices, School of
Physics, Renmin University of China, Beijing 100872, China;
orcid.org/0000-0003-2351-2060; Email: pcheng@ruc.edu.cn

Jianfeng Guo — Beijing National Laboratory for Condensed Matter Physics, Institute of Physics, Chinese Academy of Sciences, Beijing 100190, China; Email: jfguo@iphy.ac.cn

#### **Authors**

Shuo Mi – Key Laboratory of Quantum State Construction and Manipulation (Ministry of Education), School of Physics, Renmin University of China, Beijing 100872, China; Beijing Key Laboratory of Optoelectronic Functional Materials & Micro-nano Devices, School of Physics, Renmin University of China, Beijing 100872, China

Manyu Wang — Key Laboratory of Quantum State Construction and Manipulation (Ministry of Education), School of Physics, Renmin University of China, Beijing 100872, China; Beijing Key Laboratory of Optoelectronic Functional Materials & Micro-nano Devices, School of Physics, Renmin University of China, Beijing 100872, China

Bingxian Shi — Key Laboratory of Quantum State Construction and Manipulation (Ministry of Education), School of Physics, Renmin University of China, Beijing 100872, China; Beijing Key Laboratory of Optoelectronic Functional Materials & Micro-nano Devices, School of Physics, Renmin University of China, Beijing 100872, China

Songyang Li – Key Laboratory of Quantum State Construction and Manipulation (Ministry of Education), School of Physics, Renmin University of China, Beijing 100872, China; Beijing Key Laboratory of Optoelectronic Functional Materials & Micro-nano Devices, School of Physics, Renmin University of China, Beijing 100872, China

Xiaoxiao Pei – Beijing National Laboratory for Condensed Matter Physics, Institute of Physics, Chinese Academy of Sciences, Beijing 100190, China

Yanyan Geng — Key Laboratory of Quantum State Construction and Manipulation (Ministry of Education), School of Physics, Renmin University of China, Beijing 100872, China; Beijing Key Laboratory of Optoelectronic Functional Materials & Micro-nano Devices, School of Physics, Renmin University of China, Beijing 100872, China

Shumin Meng – Key Laboratory of Quantum State Construction and Manipulation (Ministry of Education), School of Physics, Renmin University of China, Beijing 100872, China; Beijing Key Laboratory of Optoelectronic Functional Materials & Micro-nano Devices, School of Physics, Renmin University of China, Beijing 100872, China

Rui Xu – Key Laboratory of Quantum State Construction and Manipulation (Ministry of Education), School of Physics, Renmin University of China, Beijing 100872, China

Li Huang – Beijing National Laboratory for Condensed Matter Physics, Institute of Physics, Chinese Academy of Sciences, Beijing 100190, China Wei Ji – Key Laboratory of Quantum State Construction and Manipulation (Ministry of Education), School of Physics, Renmin University of China, Beijing 100872, China; Beijing Key Laboratory of Optoelectronic Functional Materials & Micro-nano Devices, School of Physics, Renmin University of China, Beijing 100872, China; orcid.org/0000-0001-5249-6624

Fei Pang — Key Laboratory of Quantum State Construction and Manipulation (Ministry of Education), School of Physics, Renmin University of China, Beijing 100872, China; Beijing Key Laboratory of Optoelectronic Functional Materials & Micro-nano Devices, School of Physics, Renmin University of China, Beijing 100872, China; ⊚ orcid.org/0000-0002-8578-366X

Complete contact information is available at: https://pubs.acs.org/10.1021/acsnano.5c12067

#### **Author Contributions**

\*S.M., M.W., and B.S. contributed equally to this work. P.C., J.G., and Z.C. conceived the research project. S.M. performed the AFM and MFM experiments and analyzed the corresponding data. M.W. and X.P. performed the STM measurements. B.X. grew the single crystals. S.L., Y.G., S.M., R.X., L.H., W.J., and F.P. assisted with the experiments. S.M., J.G., and Z.C. wrote the manuscript with input from all authors.

#### **Notes**

The authors declare no competing financial interest.

## **ACKNOWLEDGMENTS**

This project was supported by the National Key Research and Development Program of China (No. 2023YFA1406500), the National Natural Science Foundation of China (NSFC) (No. 92477128, 12374200, 12074426, 12474148), the Fundamental Research Funds for the Central Universities, and the Research Funds of Renmin University of China (No. 21XNLG27), as well as the China Postdoctoral Science Foundation (No. GZC20252200, 2025M773341). This paper is an outcome of "Study of Exotic Fractional Magnetization Plateau Phase Transitions and States in Low-dimensional Frustrated Quantum Systems" (RUC24QSDL039), funded by the "Qiushi Academic - Dongliang" Talent Cultivation Project at Renmin University of China in 2024.

#### **REFERENCES**

- (1) Gong, C.; Li, L.; Li, Z.; Ji, H.; Stern, A.; Xia, Y.; Cao, T.; Bao, W.; Wang, C.; Wang, Y.; Qiu, Z. Q.; Cava, R. J.; Louie, S. G.; Xia, J.; Zhang, X. Discovery of Intrinsic Ferromagnetism in Two-Dimensional van der Waals Crystals. *Nature* **2017**, *546*, 265–269.
- (2) Burch, K. S.; Mandrus, D.; Park, J.-G. Magnetism in Two-Dimensional van der Waals Materials. *Nature* **2018**, *563*, 47–52.
- (3) Jin, C.; Kou, L. Two-Dimensional Non-van der Waals Magnetic Layers: Functional Materials for Potential Device Applications. *J. Phys. D: Appl. Phys.* **2021**, *54*, 413001.
- (4) Guo, J.; Wang, H.; Wang, X.; Gu, S.; Mi, S.; Zhu, S.; Hu, J.; Pang, F.; Ji, W.; Gao, H.; Xia, T.; Cheng, Z. Coexisting Ferromagnetic-Antiferromagnetic Phases and Manipulation in a Magnetic Topological Insulator MnBi<sub>4</sub>Te<sub>7</sub>. J. Phys. Chem. C 2022, 126, 13884–13893.
- (5) Guo, J.; Wang, H.; Zhang, H.; Mi, S.; Li, S.; Dong, H.; Zhu, S.; Hu, J.; Wang, X.; Li, Y.; Sugawara, Y.; Xu, R.; Pang, F.; Ji, W.; Xia, T.; Cheng, Z. Interlayer Coupling Modulated Tunable Magnetic States in Superlattice  $MnBi_2Te_4(Bi_2Te_3)_n$  Topological Insulators. *Phys. Rev. B* **2024**, *109*, 165410.

- (6) Mi, S.; Guo, J.; Hu, G.; Wang, G.; Li, S.; Gong, Z.; Jin, S.; Xu, R.; Pang, F.; Ji, W.; et al. Real-Space Topology-Engineering of Skyrmionic Spin Textures in a van der Waals Ferromagnet Fe<sub>3</sub>GaTe<sub>2</sub>. *Nano Lett.* **2024**, *24*, 13094–13102.
- (7) Huang, B.; Clark, G.; Navarro-Moratalla, E.; Klein, D. R.; Cheng, R.; Seyler, K. L.; Zhong, D.; Schmidgall, E.; McGuire, M. A.; Cobden, D. H.; Yao, W.; Xiao, D.; Jarillo-Herrero, P.; Xu, X. Layer-Dependent Ferromagnetism in a van der Waals Crystal Down to the Monolayer Limit. *Nature* **2017**, *546*, 270–273.
- (8) Jiang, S.; Li, L.; Wang, Z.; Mak, K. F.; Shan, J. Controlling Magnetism in 2D CrI<sub>3</sub> by Electrostatic Doping. *Nat. Nanotechnol.* **2018**, *13*, 549–553.
- (9) Deng, Y.; Yu, Y.; Song, Y.; Zhang, J.; Wang, N. Z.; Sun, Z.; Yi, Y.; Wu, Y. Z.; Wu, S.; Zhu, J.; Wang, J.; Chen, X. H.; Zhang, Y. Gate-Tunable Room-Temperature Ferromagnetism in Two-Dimensional Fe<sub>3</sub>GeTe<sub>2</sub>. *Nature* **2018**, *563*, 94–99.
- (10) Bedoya-Pinto, A.; Ji, J.-R.; Pandeya, A. K.; Gargiani, P.; Valvidares, M.; Sessi, P.; Taylor, J. M.; Radu, F.; Chang, K.; Parkin, S. S. P. Intrinsic 2D-XY Ferromagnetism in a van der Waals Monolayer. *Science* **2021**, *374*, 616–620.
- (11) Boix-Constant, C.; Jenkins, S.; Rama-Eiroa, R.; Santos, E. J. G.; Mañas-Valero, S.; Coronado, E. Multistep Magnetization Switching in Orthogonally Twisted Ferromagnetic Monolayers. *Nat. Mater.* **2024**, 23 (2), 212–218.
- (12) Telford, E. J.; Dismukes, A. H.; Lee, K.; Cheng, M.; Wieteska, A.; Bartholomew, A. K.; Chen, Y.-S.; Xu, X.; Pasupathy, A. N.; Zhu, X.; et al. Layered Antiferromagnetism Induces Large Negative Magnetoresistance in the van der Waals Semiconductor CrSBr. *Adv. Mater.* **2020**, 32 (37), 2003240.
- (13) Wang, Z.; Gibertini, M.; Dumcenco, D.; Taniguchi, T.; Watanabe, K.; Giannini, E.; Morpurgo, A. F. Determining the Phase Diagram of Atomically Thin Layered Antiferromagnet CrCl<sub>3</sub>. *Nat. Nanotechnol.* **2019**, *14*, 1116–1122.
- (14) Cai, X.; Song, T.; Wilson, N. P.; Clark, G.; He, M.; Zhang, X.; Taniguchi, T.; Watanabe, K.; Yao, W.; Xiao, D.; McGuire, M. A.; Cobden, D. H.; Xu, X. Atomically Thin CrCl<sub>3</sub>: An In-Plane Layered Antiferromagnetic Insulator. *Nano Lett.* **2019**, *19*, 3993–3998.
- (15) Telford, E. J.; Dismukes, A. H.; Dudley, R. L.; Wiscons, R. A.; Lee, K.; Chica, D. G.; Ziebel, M. E.; Han, M.-G.; Yu, J.; Shabani, S.; Scheie, A.; Watanabe, K.; Taniguchi, T.; Xiao, D.; Zhu, Y.; Pasupathy, A. N.; Nuckolls, C.; Zhu, X.; Dean, C. R.; Roy, X. Coupling between Magnetic Order and Charge Transport in a Two-Dimensional Magnetic Semiconductor. *Nat. Mater.* **2022**, *21*, 754–760.
- (16) Gao, X.; Wang, K.; Zhai, K.; Yan, J.; Yue, D.; Mu, C.; Yu, Z.; Cheng, Y.; Nie, A.; Liu, Z. Modulation of Magnetic Domain and the Occurrence of Antisymmetric Magnetoresistance in the Folded van der Waals Ferromagnet Fe<sub>3</sub>GaTe<sub>2</sub>. Adv. Mater. **2025**, 37 (27), 2420505.
- (17) Jin, S.; Liu, Y.; Deng, Z.; Wang, T.; Xu, S.; Chen, Y.; Jiang, X.; Liang, C.; Hong, J.; Cheong, S.-W.; Wang, X. Strain Gradient Induced Skyrmion in a van der Waals Magnet by Wrinkling. *Adv. Mater.* **2025**, 37 (29), 2501935.
- (18) Vishkayi, S. I.; Torbatian, Z.; Qaiumzadeh, A.; Asgari, R. Strain and electric-field control of spin-spin interactions in monolayer CrI <sub>3</sub>. *Phys. Rev. Mater.* **2020**, *4* (9), 094004.
- (19) Guo, E.-J.; Desautels, R.; Keavney, D.; Roldan, M. A.; Kirby, B. J.; Lee, D.; Liao, Z.; Charlton, T.; Herklotz, A.; Ward, T. Z.; et al. Nanoscale Ferroelastic Twins Formed in Strained LaCoO<sub>3</sub> Films. *Sci. Adv.* **2019**, *5* (3), No. eaav5050.
- (20) Du, R.; Wang, Y.; Cheng, M.; Wang, P.; Li, H.; Feng, W.; Song, L.; Shi, J.; He, J. Two-Dimensional Multiferroic Material of Metallic p-Doped SnSe. *Nat. Commun.* **2022**, *13* (1), 6130.
- (21) Wang, Y.; Wang, C.; Liang, S.-J.; Ma, Z.; Xu, K.; Liu, X.; Zhang, L.; Admasu, A. S.; Cheong, S.-W.; Wang, L.; et al. Strain-Sensitive Magnetization Reversal of a van der Waals Magnet. *Adv. Mater.* **2020**, 32 (42), 2004533.
- (22) Pal, R.; Pal, B.; Mondal, S.; Sharma, R. O.; Das, T.; Mandal, P.; Pal, A. N. Spin-Reorientation Driven Emergent Phases and

- Unconventional Magnetotransport in Quasi-2D vdW Ferromagnet Fe<sub>4</sub>GeTe<sub>2</sub>. Npj 2D Mater. Appl. **2024**, 8 (1), 30.
- (23) Feng, D.; Shen, Z.; Xue, Y.; Guan, Z.; Xiao, R.; Song, C. Strain-Induced Magnetic Phase Transition, Magnetic Anisotropy Switching and Bilayer Antiferromagnetic Skyrmions in van der Waals Magnet CrTe<sub>2</sub>. *Nanoscale* **2023**, *15*, 1561–1567.
- (24) Webster, L.; Yan, J.-A. Strain-Tunable Magnetic Anisotropy in Monolayer CrCl<sub>3</sub>, CrBr<sub>3</sub>, and CrI<sub>3</sub>. *Phys. Rev. B* **2018**, 98, 144411.
- (25) Ota, S.; Van Thach, P.; Awano, H.; Ando, A.; Toyoki, K.; Kotani, Y.; Nakamura, T.; Koyama, T.; Chiba, D. Strain-Induced Modulation of Temperature Characteristics in Ferrimagnetic Tb—Fe Films. Sci. Rep. 2021, 11 (1), 6237.
- (26) Mukherjee, T.; Chowdhury, S.; Jana, D.; Voon, L. C. L. Y. Strain Induced Electronic and Magnetic Properties of 2D Magnet CrI<sub>3</sub>: A DFT Approach. *J. Phys.: Condens. Matter* **2019**, *31*, 335802.
- (27) Ruiz, A. M.; Shumilin, A.; Dey, S.; López-Alcalá, D.; Baldoví, J. J. Tunable Itinerant Ferromagnetism in the Two-Dimensional FePd<sub>2</sub>Te<sub>2</sub> Hosting 1D Spin Chains. *arXiv*. 2025.
- (28) Shi, B.; Geng, Y.; Wang, H.; Yang, J.; Shang, C.; Wang, M.; Mi, S.; Huang, J.; Pan, F.; Gui, X.; Wang, J.; Liu, J.; Xu, D.; Zhang, H.; Qin, J.; Wang, H.; Hao, L.; Tian, M.; Cheng, Z.; Zheng, G.; et al. FePd<sub>2</sub>Te<sub>2</sub>: An Anisotropic Two-Dimensional Ferromagnet with One-Dimensional Fe Chains. *J. Am. Chem. Soc.* **2024**, *146*, 21546–21554.
- (29) Zhang, J.; Shi, B.; Xu, H.; Song, Y.; Zou, Y.; Li, Z.; Dai, H.; Song, Y.; Jin, Q.; Cheng, P.; Jin, Z.; Zhang, Z. Enhanced THz Emission and Chirality Control in van der Waals Ferromagnetic FePd<sub>2</sub>Te<sub>2</sub>/Pt Heterostructures. *J. Am. Chem. Soc.* **2025**, *147*, 19878–19885
- (30) Chen, H.; Huang, P.; Guo, D.; Xie, G. Anisotropic Mechanical Properties of Black Phosphorus Nanoribbons. *J. Phys. Chem. C* **2016**, 120, 29491–29497.
- (31) Kobayashi, S.; MartínCid, A.; Toyoki, K.; Okazaki, H.; Kawaguchi, S.; Hirosawa, S.; Nakamura, T. Effects of Texture on Lattice Constants of Nd<sub>2</sub>Fe<sub>14</sub>B and Their Relationship with Internal Stress in Nd-Fe-B permanent magnets. *Phys. Rev. Mater.* **2020**, *4*, 094405.
- (32) Chen, Z.; Yang, Y.; Guo, J.-G. Fourfold Anisotropic Magnetoresistance and Unconventional Critical Exponents in Twinned FePd<sub>2</sub>Te<sub>2</sub>. *arXiv*. 2024.
- (33) Huang, L.; Zheng, F.; Chen, H.; Thi, Q. H.; Chen, X.; Liu, H.; Lee, C.-S.; Deng, Q.; Zhao, J.; Ly, T. H. Mechanical Origin of Martensite-Like Structures in Two-Dimensional ReS<sub>2</sub>. *Commun. Mater.* **2021**, 2 (1), 87.
- (34) Yang, Y.; Xu, B.; Zong, H. Physics Infused Machine Learning Force Fields for 2D Materials Monolayers. *J. Mater. Inf.* **2023**, 3 (4), 23.
- (35) Jiang, X.; Liu, Q.; Xing, J.; Liu, N.; Guo, Y.; Liu, Z.; Zhao, J. Recent Progress on 2D Magnets: Fundamental Mechanism, Structural Design and Modification. *Appl. Phys. Rev.* **2021**, *8* (3), 031305.
- (36) Kong, D.; Kovács, A.; Charilaou, M.; Zheng, F.; Wang, L.; Han, X.; Dunin-Borkowski, R. E. Direct Observation of Tensile-Strain-Induced Nanoscale Magnetic Hardening. *Nat. Commun.* **2023**, *14* (1), 3963
- (37) Ngaloy, R.; Zhao, B.; Ershadrad, S.; Gupta, R.; Davoudiniya, M.; Bainsla, L.; Sjöström, L.; Hoque, M. A.; Kalaboukhov, A.; Svedlindh, P.; et al. Strong In-Plane Magnetization and Spin Polarization in  $(Co_{0.15}Fe_{0.85})_5GeTe_2/Graphene$  van der Waals Heterostructure Spin-Valve at Room Temperature. *ACS Nano* **2024**, *18*, 5240–5248.
- (38) Roman, A.; Gomez, J.; Butera, A.; Vavassori, P.; Steren, L. B. Magnetization Reversal and Direct Observation of Magnetic Domains on FePt Thin Films. In 2024 IEEE International Magnetic Conference Short Papers (INTERMAG Short Papers); IEEE, Rio de Janeiro, Brazil, 2024.
- (39) Milde, P.; Köhler, L.; Neuber, E.; Ritzinger, P.; Garst, M.; Bauer, A.; Pfleiderer, C.; Berger, H.; Eng, L. M. Field-Induced Reorientation of Helimagnetic Order in Cu<sub>2</sub>OSeO<sub>3</sub> Probed by Magnetic Force Microscopy. *Phys. Rev. B* **2020**, *102*, 024426.

- (40) Bigi, C.; Jego, C.; Polewczyk, V.; De Vita, A.; Jaouen, T.; Tchouekem, H. C.; Bertran, F.; Le Fèvre, P.; Turban, P.; Jacquot, J.-F.; et al. Bilayer Orthogonal Ferromagnetism in CrTe<sub>2</sub>-Based van der Waals System. *Nat. Commun.* **2025**, *16*, 4495.
- (41) Bhasker, S. U.; Choudary, G. S. V. R. K.; Reddy, M. V. R. Modulation in Magnetic Exchange Interaction, Core Shell Structure and Hopkinson's Peak with Chromium Substitution into Ni<sub>0-75</sub>Co<sub>0-25</sub>Fe<sub>2</sub>O<sub>4</sub> Nanoparticles. *J. Magn. Magn. Mater.* **2018**, 454, 349–355.
- (42) Zhu, M.; Li, P. G.; Wang, Y.; Cao, H. B.; Tian, W.; Zhang, H. D.; Phelan, B. D.; Mao, Z. Q.; Ke, X. Temperature- and Field-Driven Spin Reorientations in Triple-Layer Ruthenate  $Sr_4Ru_3O_{10}$ . Sci. Rep. **2018**, 8 (1), 3914.
- (43) Dorantes-Dávila, J.; Garibay-Alonso, R.; Pastor, G. M. Spin-Fluctuation Theory of Temperature-Driven Spin Reorientations in Ferromagnetic Transition Metal Thin Films. *Phys. Rev. B* **2024**, *110*, 174406.
- (44) Nagyfalusi, B.; Udvardi, L.; Szunyogh, L. Meta dynamics Study of the Temperature Dependence of Magnetic Anisotropy and Spin-Reorientation Transitions in Ultrathin Films. *Phys. Rev. B* **2019**, *100*, 174429.
- (45) Wang, S.; Wang, Z.; Jiang, J.; Zhang, Y.; Li, R.; Feng, Y.; Liu, P.; Lu, Y.; Sheng, Z.; Du, H.; et al. Temperature-Driven Spin Reorientation Transition in Van der Waals  $Cr_{1\cdot7}Te_2$  Ferromagnet. *Appl. Phys. Lett.* **2024**, *124* (23), 232401.
- (46) Kittel, C. Introduction to Solid State Physics; 8th ed.; John Wiley & Sons: Hoboken, NJ, 2004.
- (47) Cullity, B. D.; Graham, C. D. Introduction to Magnetic Materials; 2nd ed.; John Wiley & Sons: Hoboken, NJ, 2011.

